

# High Accuracy Non-contact Optical Flow Sensor for Monitoring Drug Delivery

Brian Catanzaro<sup>a</sup>, David Gillett<sup>b</sup>, Meghan Simmons<sup>b</sup>, Jeremy Fennelly, Burton Sage<sup>b</sup>

<sup>a</sup> CFE Services, 5147 Pacifica Dr., San Diego, CA 92109<sup>1</sup>

<sup>b</sup> TheraFuse

## ABSTRACT

External and implantable infusion pumps are deployed in an ever widening variety of therapies. These devices are continually driven to increasing accuracy, smaller size, and lower cost. One opportunity for advancement in infusion pump technology is the improvement of closed loop monitoring of the delivery dosage of pharmaceuticals. An optical flow sensor has been designed, developed, and demonstrated based on a non-contact thermal time of flight architecture. The device is a diffraction based sensor. An analytical theory of operation will be presented. Simulations were conducted using a computational model based on heat transfer and computational fluid dynamics combined with diffraction optics calculations. These simulations were corroborated by experimental observations. The sensor has been demonstrated on several prototype platforms, including a prototype using telecommunications devices and packaging technology at a size of 20 mm x 20 mm x 5 mm. Experimental results will be presented demonstrating monitoring of flow rates between 240 nl/sec to 800 nL/sec with accuracies of better than 1% CV.

Keywords: Optical sensor, flow sensing, pharmaceutical delivery, infusion pump

## 1. DRUG DELIVERY BY INFUSION

Infusion methods provide therapy for a number of situations. Diseases such as diabetes, hepatic cancer, and pain management are all served by infusion pump technology. Some systems are designed for bedside delivery. A significant portion of the delivery devices are portable and even wearable. MiniMed, Disetronic, Sorenson, and others have developed a family of pager-sized syringe pumps to serve these needs. Perhaps the best known are the insulin pumps. These systems include delivery via intravenous, arterial infusion, and even subcutaneous methods have been proposed. Size, weight, and accuracy are parameters that have a large impact on patient outcome and quality of life.

Evaluations of a variety of infusion pumps have been published, in terms of delivery accuracy, precision, battery life, and the range of pump delivery rate [1 – 4]. Infusion pump systems used for ambulatory purposes can be evaluated using AAMI testing protocols. [5] These protocols produce trumpet curves which are used specifically to characterize volumetric delivery over short and long time scales. The methodology and analysis of the trumpet curve are beyond the scope of this paper. It suffices to summarize that the accuracy goals for infusion pump systems are approximately  $\pm 3\%$  and existing technology is typically  $\pm 15\%$ .

## 2. FLOW SENSOR BASED DELIVERY

From a size, expense, and battery life point of view, a pressure based drug delivery system, where the energy needed to move the drug from a reservoir to the patient is provided by mechanical pressure, and not by electrical machinery, would be preferable. But compared to the accuracy achievable by positive displacement systems such as the syringe pump and the peristaltic pump, pressure based systems have difficulty competing in open loop configurations. Pressure variations as the reservoir empties, viscosity variations with temperature, and flow path geometry variations from infusion set to infusion set when combined over the range of intended uses can introduce delivery rate errors in excess of 100%.

One approach for improving the accuracy of a pressure based system is to combine the pressurized reservoir with a flow sensor and a flow regulator. The flow sensor measures the actual flow rate and works with the flow regulator in closed

---

<sup>1</sup> Correspondence - Email: [bcatanza@alumni.caltech.edu](mailto:bcatanza@alumni.caltech.edu); Telephone: 858-204-6299

loop fashion to provide the selected flow profile over a wide range of operating conditions. In such a system, flow is started and measured by the sensor. Based on the output of the flow sensor, the flow rate is adjusted using the flow regulator. This process of flow measurement and flow adjustment continues until the desired flow rate is achieved. After the selected flow rate is achieved, monitoring continues over the delivery episode, and changes are made as necessary to compensate for delivery variation that may occur due to changes in temperature, infusion set, pressure drop, occlusion, and amount of drug remaining.

The proposed system consists of a pressurized reservoir, an open/close valve, a flow sensor, and a simple microprocessor. The reservoir is pressurized using a mechanical fixed spring. The valve is a simple open/close valve that regulates flow using a pulse width modulated scheme. The flow sensor is based on a non-contact, optical time of flight measurement. The key advantages of this method include:

- Non-contact measurement of flow rate,
- Direct monitor of dosage delivered to the patient,
- Low cost/low power drive mechanism for delivering dose,
- Dramatic reduction in system size and cost,
- Enables disposable systems which improve reliability.

### 3. OPTICAL TIME OF FLIGHT PRINCIPLE

The concept of the time of flight sensor is the monitoring of the time required for an event related to the velocity of the liquid to travel between two points. After experimenting with a variety of configurations, an optical time of flight configuration was optimized. The principle of operation of this configuration will be described. The methodology and results of simulations of this configuration will be presented. In addition, experimental data verifies the principle of operation as well as the simulations.

#### 3.1 Principle of Operation

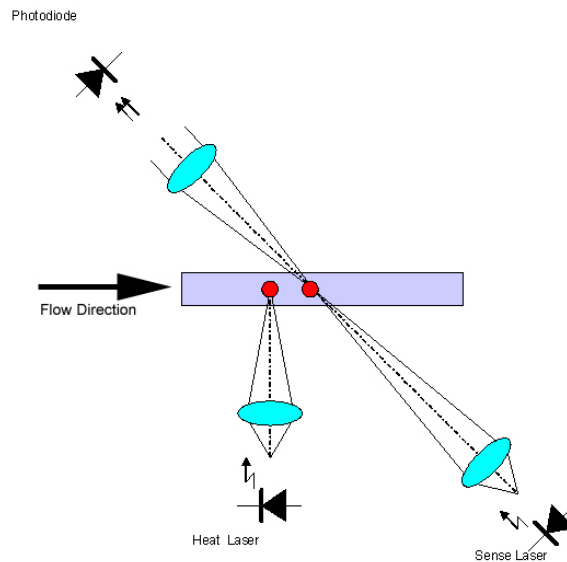


**Figure 1: Schematic of Time of Flight Sensor**

The time of flight sensor is based on laser heating a small section of fluid in a capillary and timing the transit of this heated bolus (see Figure 1). The laser used to heat the fluid has a wavelength centered near 1490 nm. This wavelength was chosen based on the availability of inexpensive, relatively powerful lasers (> 100 mW) at this wavelength as well as the absorption coefficient of water at this wavelength: 19/cm (see Figure 2). This laser was focused onto a section of a

narrow capillary (50 μm x 50 μm cross section). Water exhibits a significant change in index of refraction near ambient temperature (see Figure 2). The fluid is heated by absorption of the laser energy, inducing a change in the index of refraction.

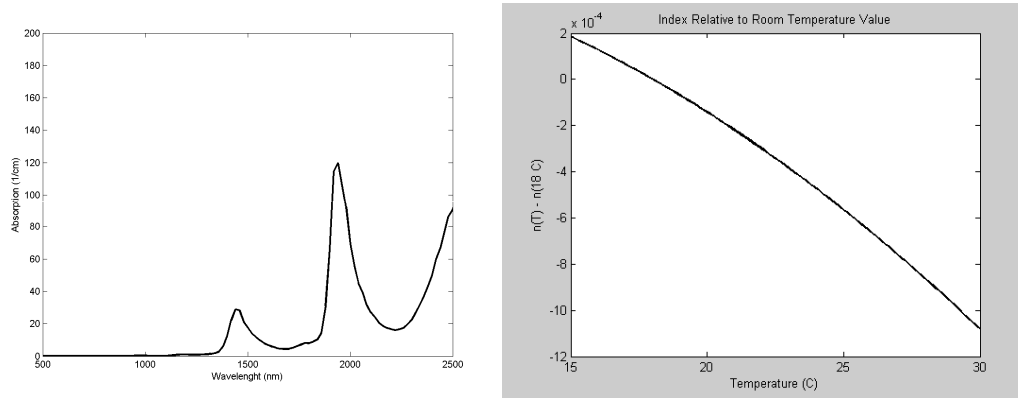


**Figure 2: Water Absorption Spectra (left) and Water Index of Refraction as a Function of Temperature Relative to Room Temperature (right)**

This thermal profile propagates downstream by advection. Although the temperature distribution changes as it propagates, a localized thermal profile still exists several hundred microns downstream. Illuminating the capillary with a visible laser (635 nm) light can reveal the presence of the temperature distribution (see Figure 3). The localized change in temperature produces a localized index change. This localized index profile perturbs the wavefront of the illumination. This diffracts the incident beam, reducing the Strehl ratio of the focused beam.

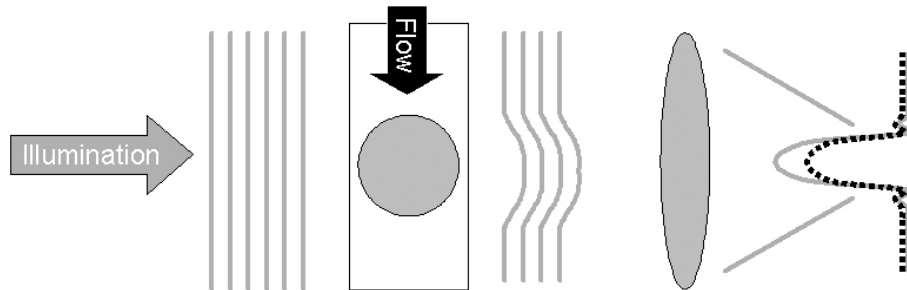


**Figure 3: Diffraction from the Localized Heating of the Fluid is Detectable as a Reduction in Strehl Ratio**

### 3.2 Analysis of Effect

The diffraction effect is visible in both the far field and the near field. A far field analysis is possible with some simplifying assumptions. The expression for the amplitude of the optical field in the far field is:

$$\tilde{U}_{far} = \frac{1}{\lambda z} \exp[ikz] \exp\left[i \frac{k}{2z} (x^2 + y^2)\right] \iint U_{in}(\xi, \eta) \exp\left[-i \frac{k}{z} (\xi x + \eta y)\right] d\xi d\eta$$

where  $k$  is the wavenumber,  $\lambda$  is the wavelength,  $z$  is the propagation distance (capillary to detector), and  $U_{in}$  is the input optical field.

The intensity can be calculated from the optical fields. The optical fields can be calculated using superposition. Using rectangular profiles for phase and amplitude:

$$U_{cold} = \text{rect}\left(\frac{x}{D_x}\right)\text{rect}\left(\frac{y}{D_y}\right), U_{hot} = U_{cold} + (e^{i\phi} - 1) \times U_{bolus},$$

$$U_{bolus} = \text{rect}\left(\frac{x}{d_x}\right)\text{rect}\left(\frac{y}{d_y}\right), \phi = \Delta n \times kt$$

where  $U_{cold}$  is the optical field over the illumination region,  $U_{bolus}$  is the optical field over the bolus region,  $\phi$  is the optical phase change induced by heating the bolus,  $\Delta T$  is the difference in temperature between the bolus and the surrounding fluid,  $dn/dT$  is the change in index as a function of temperature,  $k$  is the wavenumber, and  $t$  is the thickness (optical path length) through the fluid.

If the detector is placed in the far field, then the intensity at the center ( $x = 0$ ;  $y = 0$ ) can be calculated by using the Fourier Transform of the input optical fields. The fields at the detector can be used to calculate the ratio of the intensity of the hot and cold signal:

$$m = \frac{I_{hot} - I_{cold}}{I_{cold}} = \frac{|\tilde{U}_{hot}|^2 - |\tilde{U}_{cold}|^2}{|\tilde{U}_{cold}|^2},$$

$$\tilde{U}_{cold}\big|_{x=0,y=0} = \frac{\exp(ikz)}{i\lambda z} D_x D_y, \tilde{U}_{hot}\big|_{x=0,y=0} = \frac{\exp(ikz)}{i\lambda z} (D_x D_y + (e^{i\phi} - 1) \times d_x d_y),$$

$$m = 2(\cos \phi - 1) \left( \frac{d_x d_y}{D_x D_y} - \left( \frac{d_x d_y}{D_x D_y} \right)^2 \right) = 2(\cos \phi - 1) \left( \frac{a}{A} - \left( \frac{a}{A} \right)^2 \right)$$

$$\text{where } A \equiv D_x D_y \text{ and } a \equiv d_x d_y.$$

The modulation can be maximized given certain conditions:

1.  $\phi = \frac{\pi}{2}$ , or

2.  $\frac{a}{A} = \frac{1}{2}$ .

Given the temperature range, it is unlikely that the phase will reach  $\pi/2$ . For  $\Delta T = 10$  C,  $\Delta n = -0.9396$ . For a thickness of  $t = 50$   $\mu\text{m}$ , the phase delay ( $\phi$ ) is  $0.0740 \lambda$  or  $464$  mrad. Given this small phase delay, the modulation can be approximated as:

$$m \cong \phi^2 \left( \frac{a}{A} - \left( \frac{a}{A} \right)^2 \right) \leq \frac{\phi^2}{4} = 0.054 = 5.4\% .$$

Upon further inspection, this relationship holds true for any bolus profile that has a constant phase over the extent of the bolus. The field strength at the origin of the output field is proportional to the average field strength of the input field multiplied by the size of the field:

$$\tilde{U}_{far}(0,0) = \frac{1}{\lambda z} \exp[ikz] \iint U_{in}(\xi, \eta) d\xi d\eta = \frac{A}{\lambda z} \exp[ikz] \langle U_{in} \rangle.$$

Therefore, regardless of whether the field is elliptical, Gaussian, or rectangular as long as the phase is constant across the bolus, the results will be the same.

### 3.3 Computational Simulation

The analytical model is instructive in explaining the basis of the effect. However, the heat transfer and fluid dynamics of the time of flight sensor cannot be captured using simple analytical expressions. Instead, a computation model was developed to simulate the time of flight sensor. This model used a combination of two simulations: a computational fluid dynamics (CFD) model that incorporated heat transfer and an optical simulation of the diffraction.

The CFD model was implemented using CFDRC. This tool allowed for solution to both the fluid dynamics and heat transfer of the time of flight sensor. The flow rates combined with the geometry result in a laminar flow condition. Therefore, CFDRC was used to first establish a steady state flow of 475 nl/sec. Using user subroutines, a heat source was created that represented Gaussian illumination (beam waist of 50 μm x 35 μm) absorbed in the water using Beer’s law. The transient heat transfer solver was then used in conjunction with the laminar flow solver to compute the evolution of temperature over time and space.

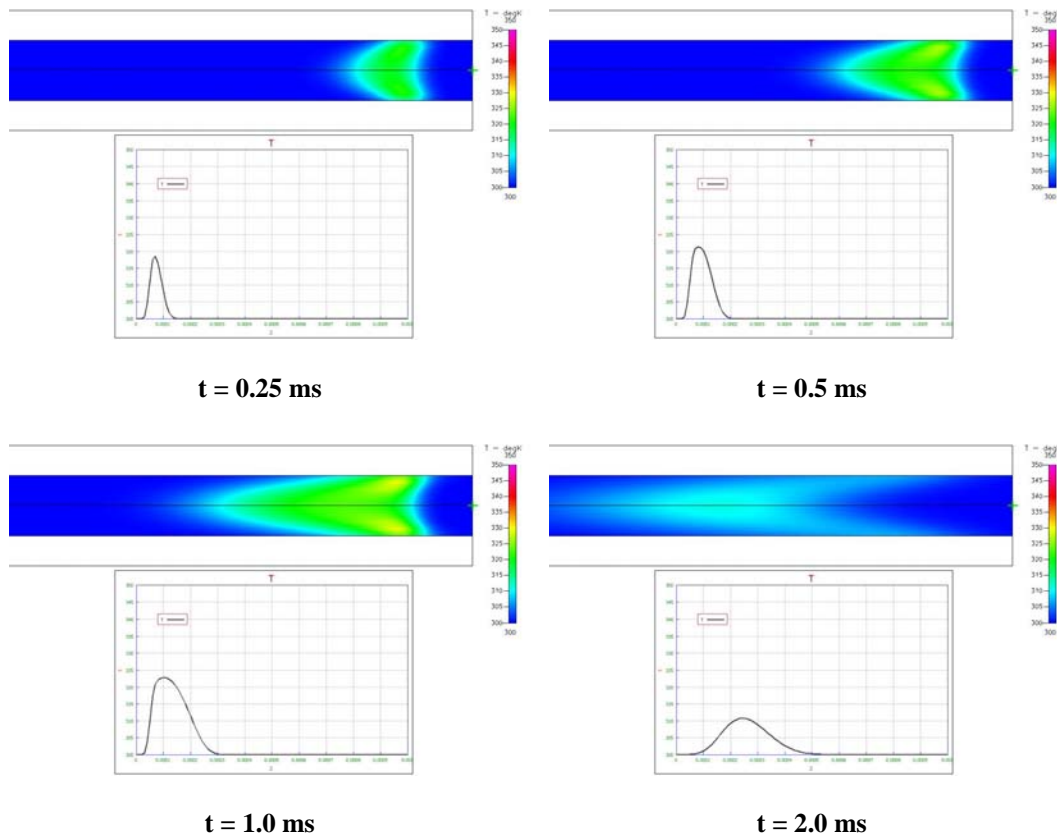


**Figure 4: CFD/Heat Transfer Simulation Results Using CFDRC**

The power emitted from the heat laser was modeled as 400 mW. The exposure time of the laser was 1 msec. Figure 4 shows a cross section through capillary over a 2 ms time period. The simulation shows the temperature map as a contour across the cross section of the capillary tube in a plane perpendicular to the direction of the heat laser propagation. Below each contour is a temperature profile through the centerline of the capillary.

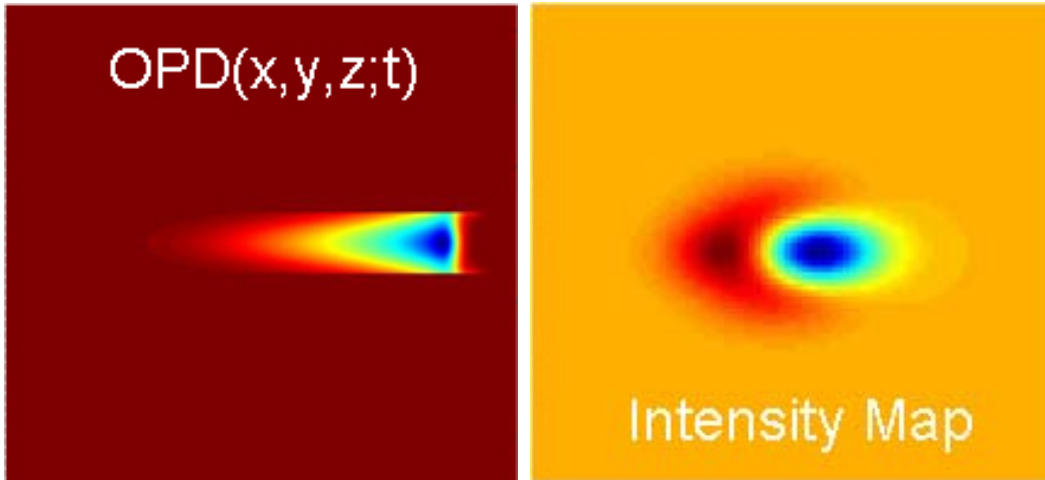


**Figure 5: OPD Map from Temperature Profile and Far-Field Intensity Pattern**

The temperature distribution was integrated along the optical axis of the sense laser, producing an optical path difference (OPD) map (see Figure 5). The OPD was then converted to a far field pattern using a standard FFT computation. Using this methodology, the peak temperature increase over ambient was  $\Delta T = 25$  C modulation (m) was 10%.

### 3.4 Experimental Measurements

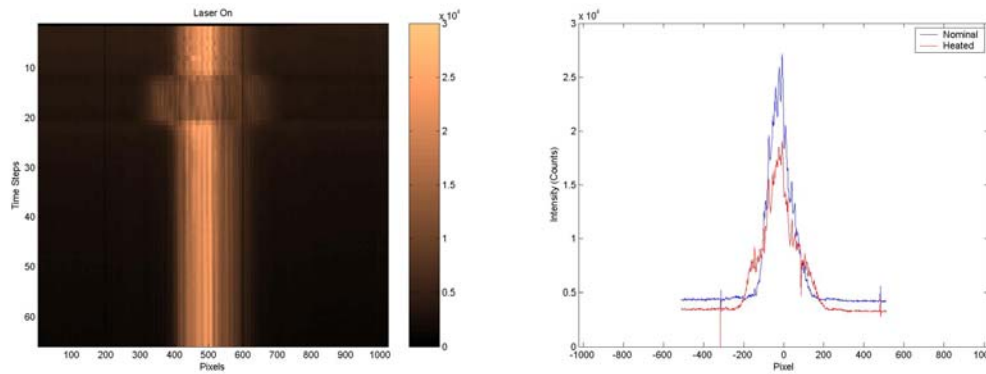


**Figure 6: Measurements of the Diffracted Signal from the Time of Flight Sensor – Linescan Camera Output (left), Intensity Profile for Nominal and Heated Fluid in the Capillary**

Using a high speed linear CCD camera, the time and space evolution of the signal diffracted from the time of flight sensor was measured. Figure 6 shows the output of the line scan camera as a function of time. On the left, each horizontal line represents a single time step in the measurement with the horizontal axis representing the spatial distribution of the intensity of the diffracted pattern. On the right, two single time steps are isolated. The blue line illustrates the far field pattern for the capillary at ambient temperature. The red line illustrates the response to illuminating the heated bolus. Note the reduction in the peak intensity and the superposition of two Gaussian profiles – one broad and the other narrow. The width of the broad profile indicates the lateral size of the bolus while the decrease in peak intensity (Strehl ratio) indicates the temperature of the bolus. This measurement indicates a  $\Delta T$  of 19 C as compared to the simulation which indicates a peak temperature increase of 25 C.

#### 4. TIME OF FLIGHT SIGNALS

The time of flight reveals the flow rate through the system:

$$Q = \frac{A d_{spot}}{t_f},$$

where  $Q$  is the flow rate,  $A$  is the cross section area of the capillary,  $d_{spot}$  is the distance between the heat laser and the sense laser spot, and  $t_f$  is the time of flight. The complex signals described in the previous section must be reduced to a simple time of flight value to be useful. Using a center of mass computation (see Figure 7) for the time of flight enabled the system to become robust to noise, reducing the jitter in the signal.

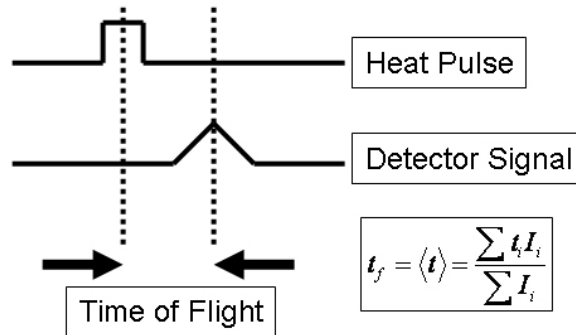


**Figure 7: Time of Flight Computation**

An ensemble of ten (10) detector signals for 800 nl/sec and 240 nl/sec are shown in Figure 8. The coefficient of variance for the time of flight for these signals is 0.07% and 0.4% respectively. Note that at the slower flow rate (right) the peak takes longer to arrive in front of the sense laser spot and the width of the signal has broadened.

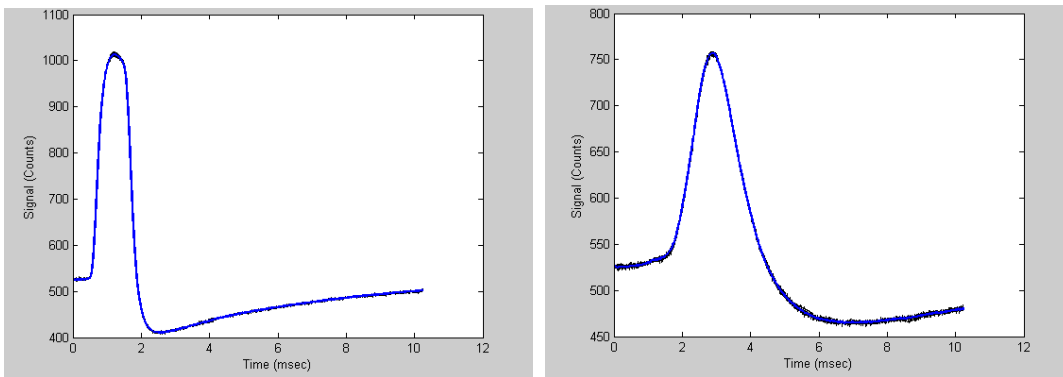


**Figure 8: Detector Signals for 800 nl/sec (left) and 240 nl/sec (right) Flow Rates**

The time of flight sensor was combined with a pulse width modulated valve. The system was calibrated using a precision gravimetric scale. The flow rate as a function of time of flight is shown in Figure 9. As expected, the flow rate is approximately proportional to  $1/t_f$ . For improved accuracy, the data was fit to a second order polynomial. As shown in Figure 9, errors are dramatically reduced by incorporating this second order term.

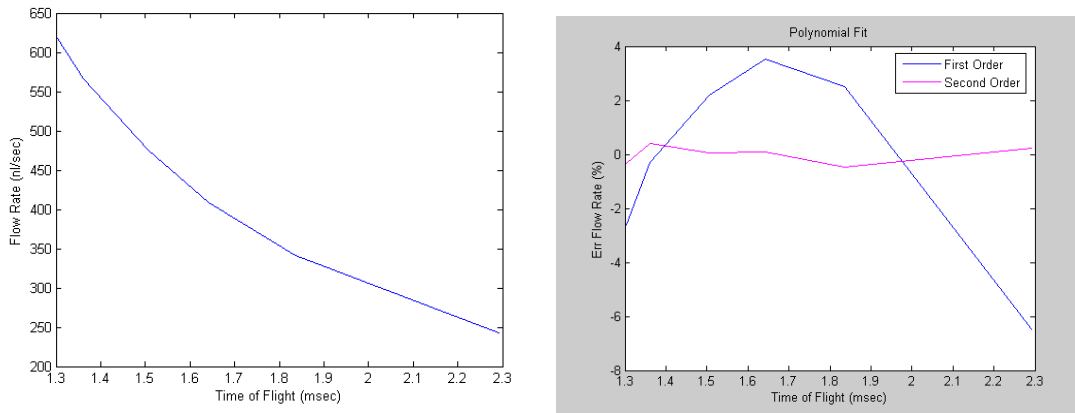


**Figure 9: Flow Rate as a Function of Time of Flight (left), Calibration Errors for a First and Second Order Fit**

Once the system was calibrated, it was operated to deliver a constant flow rate under various pressure conditions. Figure 10 shows the accuracy of delivery. The coefficient of variance of this delivery set was 0.94%.

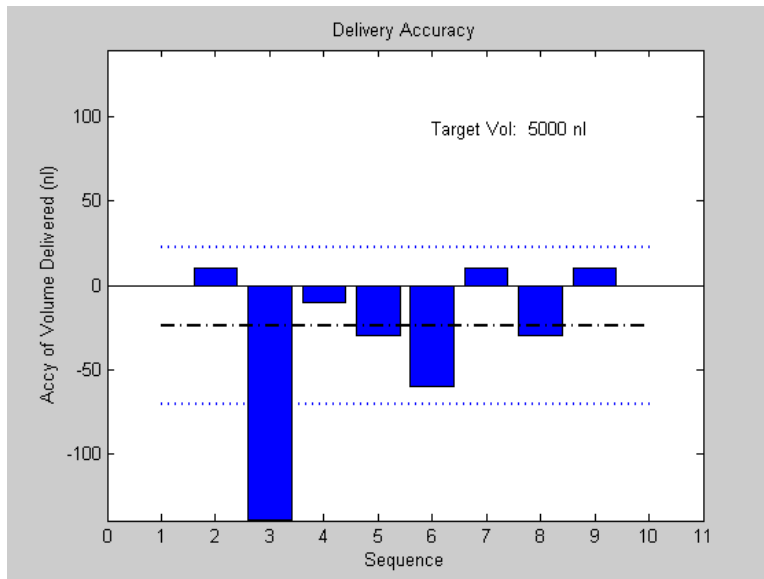


**Figure 10: Delivery Accuracy of Time of Flight Sensor Closed Loop System**

## 5. IMPLEMENTATION PLATFORMS

The time of flight sensor was combined with a valve and microprocessor to create a dose delivery system. This system was implemented on two separate platforms: a brassboard and an integrated opto-electronic prototype.

### 5.1 Brassboard Platform

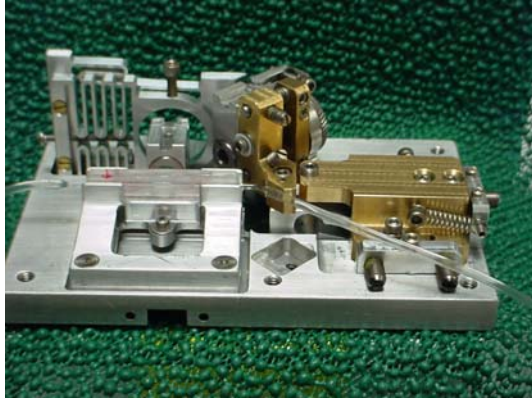
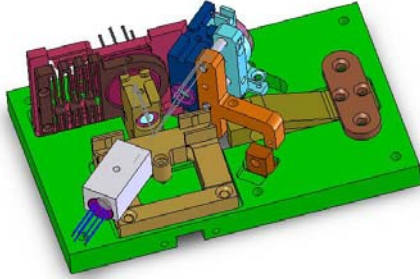


**Figure 11: Brassboard Time of Flight Sensor**

The brassboard prototype (see Figure 11) took the system from the benchtop to a portable platform (150 mm x 100 mm x 75 mm) suitable for animal trials. The brassboard integrated packaged COTS laser diodes, COTS biconvex, aspheric lenses, with machined aluminum housings. The system was tethered to power supply, but was otherwise fully autonomous. The brassboard sensor was designed to be realigned. As such, a combination of slides, flexures, and threaded housings were used to provide travel in various directions. These mechanisms accounted for the majority of the mass and volume of the brassboard. The time of flight data presented in the previous section was produced using this brassboard prototype.

The prototype was used in an animal study. [6] The study compared COTS pump technology to the delivery system based on the time of flight sensor. In the study, the time of flight system outperformed the pump with an average error of 8.58% as compared to 24.55% for the pump.

### 5.2 Integrated Opto-Electronic Prototype

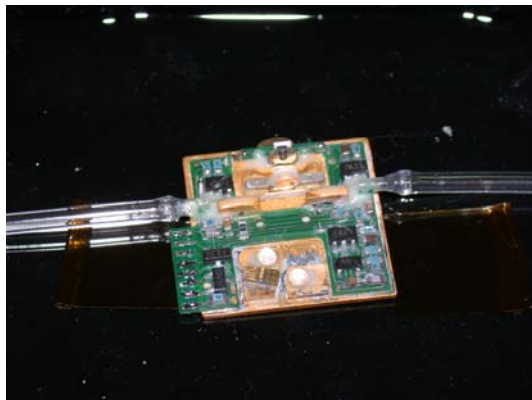
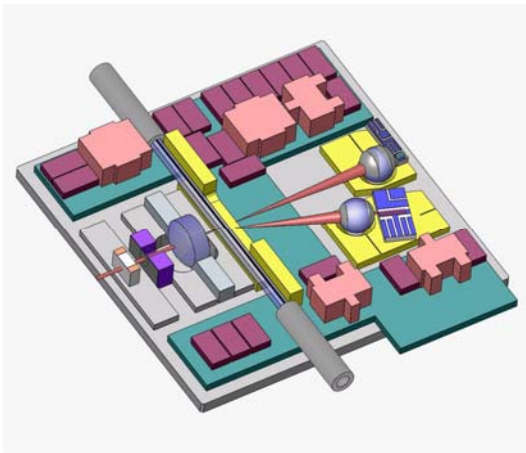


**Figure 12: Integrated Opto-Electronic Time of Flight Sensor Prototype**

In order to reduce the size and cost of the sensor, it was redesigned to leverage components and assembly techniques developed for the telecommunications industry (see Figure 12). The resulting size of the sensor was 20 mm x 20 mm x 5 mm. The sensor used bare laser die packaged on ceramic and cover substrates. The optics consisted of ball lenses and a single plano-convex lens. The detector was bare silicon die. This proof of concept platform was used to demonstrate time of flight signals.

## 6. SUMMARY

A novel flow sensor based on non-contact optical time of flight has been described. The principle of operation is supported by analytical and computational models that are confirmed with experimental observations. The time of flight signals demonstrate a very low coefficient of variance ( $< 1\%$ ) over a wide range of flow rates (240 nl/sec – 800 nl/sec). Two hardware platforms that have been integrated with valves and microprocessors have been described. These systems represent the promise of a smaller and more accurate pharmaceutical delivery system than is currently available.

The authors wish to thank the Prof. Dorian Liepmann (UCB) as well as David Mun (M.S. UCB) for their consultation and contribution to the creation of the CFD model.

## 1. REFERENCES

1. D. Capes, K. Martin, and R. Underwood “Performance of a restrictive flow device and an electronic syringe for continuous subcutaneous infusion,” *J Pain Symptom Manage.* 1997 Oct; 14(4):210-7.
2. DF Veal, CE Altman, BT McKinnon, and O. Fillingim “Evaluation of flow rates for six disposable infusion devices,” *Am J Health Syst Pharm* 1995 Mar 1;52(5):500-4.
3. M Valente, JA Aldrete “Comparison of accuracy and cost of disposable, nonmechanical pumps used for epidural infusions,” *Reg Anesth.* 1997 May-Jun;22(3)260-6.
4. BM Ilfeld, TE Morey, and FK Enneking “Portable infusion pumps used for continuous regional analgesia: delivery rate accuracy and consistency,” *Reg Anesth Pain Med.* 2003 Sep-Oct;28(5):424-32.
5. AAMI Standard AAMI ID26:1998. Medical Electrical Equipment—Part 2: Particular Requirements for the safety of infusion pumps and controllers. Assoc. for the Advancement of Medical Instrumentation 1999 Arlington, VA.
6. M. Simmons, D. Gillett, B. Catanzaro, B. Jacobs, B. Sage “A Closed Loop Drug Infusion System,” *Diabetes Technology and Therapeutics*, Vol 6 (5) 2004.